Optimization and Performance Analysis of BLDC Motors Using the FEM Simulations

Alireza Siadatan, SMIEEE
EECS Department, York University, CA.
siadatan@yorku.ca

Hamed Karimi, SIEEE
Optimized Motor Solutions Inc., CA
h.karimi@khatam.ac.ir

Moyang Cui,
ECE Department,
UofT, CA
sebastian.cui@mail.utoronto.ca

Fatemeh Ghalavand,
ECE Department,
University of Victoria, BC, CA.
fghalavand@uvic.ca

Amirhosein Mansouri
Optimized Motor Solutions Inc., CA
a.mansouri@mail.sbu.ac.ir

Maryam Sepehrinour,
ECS Department,
Algoma University,
Brampton Campus, CA.
maryam.sepehrinour@algomau.ca

***Abstract*—This paper provides a comprehensive analysis of Brushless DC Motors (BLDC), emphasizing design methodologies for optimal performance in applications like automotive, industrial, and personal transportation devices. A robust design and optimization approach using Taguchi method to reduce and minimize the tooth torque and improve the operational efficiency is also designed using broadband modulation method for speed control. The motor's stator and rotor designs, including precise calculations for parameters like outer diameter, tooth size, and magnetic loadings, are meticulously detailed, ensuring alignment with nominal performance specifications. Finite Element Methods (FEM) simulations validate key performance indicators such as torque, back-electromotive force (B-EMF), and efficiency, while comparing different motor configurations. Additionally, thermal and mechanical analyses are conducted to assess reliability under varied load conditions. The findings confirm that the optimized BLDC motors align closely with design targets, achieving high efficiency and stability, making them viable for applications demanding precise control and energy efficiency.**

Keywords—Brushless DC Motor, Design Optimization, Finite Element Method, Torque Control

I. INTRODUCTION

BLDC motors are widely used in automotive, pumping, smart devices, and electric vehicles, and are expected to replace induction motors by 2030 due to their high efficiency, durability, and low maintenance [1]. Recent research has improved BLDC design and control, including Taguchi-based optimization to reduce cogging torque and improve torque output [2], low-cost microcontroller control methods for industrial use [3], and Hall-sensor-based control systems for cost-effective applications in home appliances and automotive systems [4].

A five-phase BLDC motor specifically designed for electro hydrostatic actuation systems was presented, emphasizing its compact structure and fault tolerance. Evaluations of its thermal behavior and reliability were conducted [5]. Furthermore, a cost-effective BLDC motor solution for residential water pumps was proposed, achieving better energy efficiency through optimized control of torque and speed [6]. In the realm of electric vehicle applications, a robust optimization algorithm for BLDC motors was established, taking into account manufacturing tolerances and driving cycles, with validation supported by experimental data and FEM analysis [7]. The Taguchi method was also applied to optimize motor designs for electromobility propulsion, comparing both exterior and interior rotor configurations regarding efficiency and material usage [8]. For drone delivery systems, design considerations for BLDC motors were examined, optimizing elements like the stator and rotor to attain high torque and efficiency in heavy-load scenarios [9]. Lastly, a novel state-filtering system was introduced for BLDC motors, enhancing closed-loop position control through the direct use of high-order state derivatives. This system demonstrated superior precision when validated against conventional observers and filters [10].

In this study, the design and analysis of a BLDC motor are detailed, focusing on critical design parameters such as output power, voltage, speed, and torque. The motor's stator design involves calculating dimensions like the outer and inner diameters and tooth sizes, utilizing equations for magnetic and electrical loadings to ensure optimal performance. The air gap length is determined to maintain magnetic efficiency, and a fixed rotor-to-stator diameter ratio is established for the four-pole motor. FEM analysis is essential in BLDC motor studies, as it enables accurate evaluation of electromagnetic performance and local flux distribution that cannot be captured precisely through analytical sizing equations alone [11]. FEM are employed for simulating the motor's performance, analyzing parameters such as torque, cogging torque, and B-EMF, leading to the selection of the best-performing motor designs.

II. BLDC MOTOR DESIGN

Each electric motor has specific nominal values corresponding to its application. Therefore, some design assumptions are summarized in TABLE 1.

TABLE 1. DESIGN ASSUMPTIONS.

Parameter	Value	Unit
Output Mechanical Power	250	W
Voltage Source	48	V
Nominal Speed	200	RPM
Nominal Torque	12	N.M

The stator design includes calculating the outer diameter, inner diameter, and the dimensions of the teeth [12].

$$P = C_O.L_W \tag{1}$$

Here P is the motor output power (W), D is the motor diameter (m), L is the motor axial length (m), w is the motor speed (rad/s), and C_O is calculated from (2):

$$C_O = 10.9624\,(B_{av}.ac.k_{sw}) \tag{2}$$

979-8-3315-8138-1

While B_{av} is the average air-gap magnetic loading (T), ac is the specific electric loading (A/m), and k_{sw} is the winding factor. The winding factor represents the effect of the winding distribution and skew on the induced EMF; for an ideal motor with properly selected slots and no skew, it is typically assumed to be 1.

The magnetic loading B_{av} depends on the permanent magnet properties and is commonly estimated as the product of the magnet coverage factor per pole and the residual flux density of the magnet material. The electrical loading ac is usually selected based on empirical design guidelines and practical experience [13–14]. After calculating C_0, from eq. (2) and substituting in eq. (1), and considering the known values of motor output power and speed, the main sizing relationship is obtained as:

$$D_0^{\,2} L = K \tag{3}$$

III. MODEL AND EXPERIMENT DESIGN

In this case, a ratio between the motor diameter and its axial length is considered based on design considerations. As a result, the stator's outer diameter and the motor's axial length will be calculated accordingly.

Assuming that the magnetic flux produced by the magnet follows the path shown in Fig .1, the motor's equivalent magnetic circuit will be as shown in Fig .2. It should be noted that the leakage inductance is neglected in this case. According to Fig .2, the flux passing through the air gap is equal to the flux passing through the stator tooth. From this principle, the stator tooth width can be calculated.

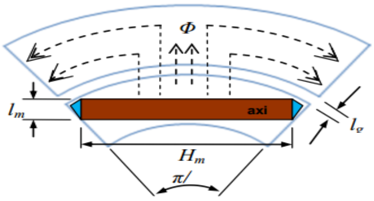

Fig. 1. Magnetic Flux Path.

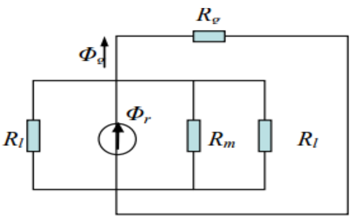

Fig. 2. Equivalent Magnetic Circuit.

$$A_t B_t = A_g B_g \tag{4}$$

Assuming that the magnetic flux produced by the magnet follows the path shown in Fig. 1, the motor's equivalent magnetic circuit will be as shown in Fig. 2. The flux passing through the air gap is equal to the flux passing through the stator tooth. From this principle, the stator tooth width can be calculated.

$$b_{ts} K_{st} L B_t = 2\pi R_g L B_g \rightarrow b_{ts} = \frac{2\pi R_g B_g}{K_{st} B_t} \tag{5}$$

Where A_t is the cross-sectional area of the stator tooth (m^2), A_g is the cross-sectional area of the air gap (m^2), B_t is the flux density of the stator tooth (T), B_g is the flux density of the air gap (T), R_g is the average radius of the air gap, and K_{st} is the filling factor of the stator core sheets. The air gap flux density is obtained from (6) [15]:

$$dg = \frac{K_l C_\varphi}{1+\dfrac{K_r \mu_r}{P_c}} B_r, P_c = \frac{lm}{gC\varphi}, C\varphi = \frac{Am}{Ag} \tag{6}$$

In this equation, C_ϕ is the ratio of the magnet cross-sectional area to the air gap cross-sectional area, B_r is the residual flux density of the magnet (T), K_l is the leakage coefficient, which ranges from 0.9 to 1, K_r is the reluctance factor, which ranges from 1 to 1.2, μ_r is the magnetic permeability of the environment, and P_c is the permeance (Wb/A). Typically, a value is considered for the stator tooth flux density based on the saturation point of the material used in the core. After calculating the air gap flux density from (6) and substituting it into (5), the stator tooth width will be calculated. Assuming that half of the flux generated by each magnet passes through the stator yoke, [16]:

$$h_{sy} K_{st} L B_{sy} = \pi RgLBg \rightarrow bts = \frac{\pi RgBg}{KstBsy} \tag{7}$$

A similar method can be used to calculate rotor width. In designing a permanent magnet synchronous motor, a fixed ratio between the rotor and stator outer diameters is considered. This ratio varies depending on the number of motor poles, and for a four-pole motor, it is 0.55.

$$Dr = 0.55Do \tag{8}$$

1- Model of the Motor

Where D_r is the rotor outer diameter. Additionally, the stator inner diameter is equal to the rotor outer diameter plus the air gap thickness. Therefore, with the air gap thickness known, the stator inner diameter can be calculated. In eq. (8), D_r is the rotor's external diameter. On the other hand, the internal diameter of the stator equals the external diameter of the rotor plus the thickness of the air gap. Therefore, by knowing the air gap thickness, the internal diameter of the stator can be calculated. In synchronous machines, the air gap length is typically determined based on the permissible armature reaction. The armature reaction should not significantly reduce the air gap magnetic field. In other words, the field winding current must be greater than the armature current. The air gap length is determined by eq. (9).

$$g = \gamma \tau p \frac{ac}{Bg} \tag{9}$$

B_g is the maximum air gap flux density (T), γ is 4×10^{-7} for salient poles and 3×10^{-7} for smooth poles [17]. Given the non-uniformity of the air gap, the calculated air gap should be multiplied by a coefficient called the Carter coefficient [18]. This coefficient is determined by eq. (10).

$$Kc = \left[1 - \frac{1}{\frac{\tau s}{Ws}\left(5\frac{g}{Ws}+1\right)} \right]^{-1} \tag{10}$$

2- Plan the Experiment

The previous section reviewed the analytical design methods and calculations for the motor dimensions. This section focuses on the design of the motor itself. The number of poles is set at 4, but the number of slots is not fixed. The design examines all possible configurations for a 4-pole BLDC motor, with TABLE. 2, showing the possible slot numbers for a 4-pole motor.

979-8-3315-8138-1

TABLE. 2. shows the possible pole-slot combinations.

Number of Poles	4	4	4	4	4	4	4	4	4
Number of Slots	9	12	15	18	21	24	27	30	33

The outputs of the designed motors, such as torque, input power, output power, and efficiency, are shown in TABLE. 3. The final motor will be fully analyzed in the simulation chapter [19]. Based on the output table, the designed motors have values close to the nominal values considered for the motor.

TABLE. 3. Provides the motor outputs.

Motor Model	Torque (N.m)	Losses (Kw)	Output Power (Kw)	Efficiency (%)
33-4	12.9	0.0327	0.271	89.2
30-4	12.8	0.0317	0.268	89.4
27-4	12.3	0.0298	0.258	89.6
24-4	12.8	0.0315	0.268	89.5
21-4	12.4	0.0302	0.26	89.6
18-4	12.3	0.0307	0.258	89.4
15-4	12	0.0293	0.251	89.5
12-4	12.4	0.0309	0.259	89.3
9-4	12.5	0.032	0.261	89.1

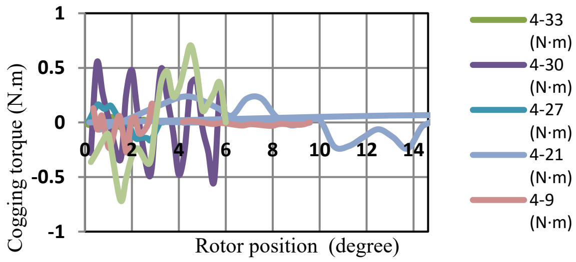

Fig. 3. Tooth diameter.

TABLE 4. Torque ripple of different structures.

Motor Model	Torque Ripple (N.m)
9-4	4.3
12-4	8.98
15-4	3.3
18-4	7.87
21-4	3.3
24-4	2.9
27-4	2.3
30-4	3
33-4	2.8

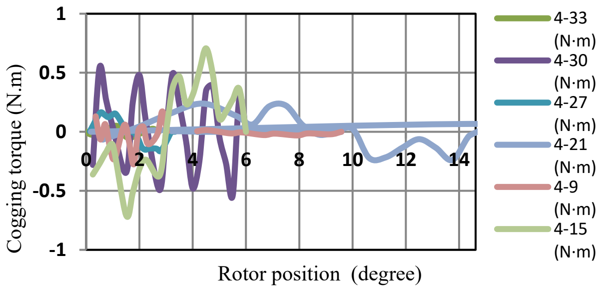

Fig. 4. Gear torque.

As mentioned earlier, cogging torque is an unwanted parasitic torque, and its maximum value should be less than 5% of the nominal torque. To calculate this torque, the stator windings are unenergized, and the rotor is rotated at a low speed. The resulting torque is the cogging torque, as shown in Fig. 3, with the maximum values listed in TABLE 4.

TABLE. 5. Gear torque range.

Motor Model	Cogging Torque (N.m)
9-4	0.275
15-4	0.707
21-4	0.239
27-4	0.127
30-4	0.542
33-4	0.0507

The phase-to-phase voltage for three motors is shown in Fig. 4. The B-EMF of these motors is similar, with minor differences. indicating that all motors except the 4-9 model have very low harmonics, resulting in the elimination of the 4-9 motor. The torque-speed curves of the remaining motors are shown in Fig. 5. All motors produce nominal torque up to a speed of 1600 RPM, after which the torque decreases.

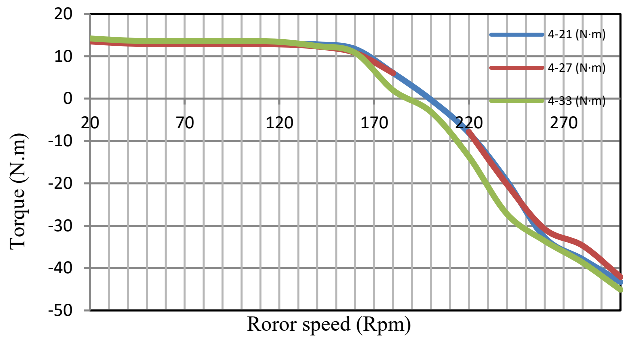

Fig. 5. Torque curve according to speed.

IV. Finite Element Analysis of The Studied BLDC Motor

FEM was initially used for structural analysis problems and started being applied in heat transfer and fluid flow problems in the early 1950s. In 1970, a paper titled "Solving Saturable Magnetic Field Problems Using the Finite Element Method" opened a new horizon in applied electromagnetism, allowing the formulation of problems with complex geometries and nonlinear magnetic properties. Nowadays, with the emergence of machines with complex geometries, the use of this tool has become inevitable. Traditional machine analysis methods were often accompanied by many assumptions to reduce computational difficulties, leading to limitations in accuracy [20]. However, FEM allows achieving high accuracy without the need for many assumptions. In this part, the simulation of the motor designed in the previous chapter will be examined, and the simulation results will be compared with the analytical results. The analyses in this section were carried out using Flux software, which is one of the most accurate software tools for FEM. Meshing the motor geometry: After defining the different regions of the motor, we mesh the structure. The meshed structure of the motor under study is shown in Fig. 6. It is clear from this figure that critical areas in the motor, such as the magnet and air gap, have a higher mesh density compared to other parts.

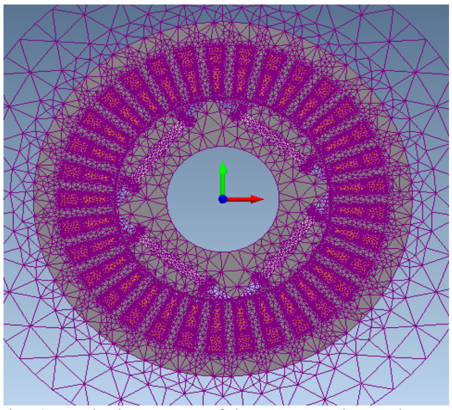

Fig. 6. Meshed structure of the motor under study.

The flux density distribution and flux path of the motor are shown in Fig. 7. According to this figure, the flux density at the hot spot of the stator is about 2.19 T. Additionally, it can be seen that the core flux density is around 1.6 T, which is below the saturation level of the core [21].

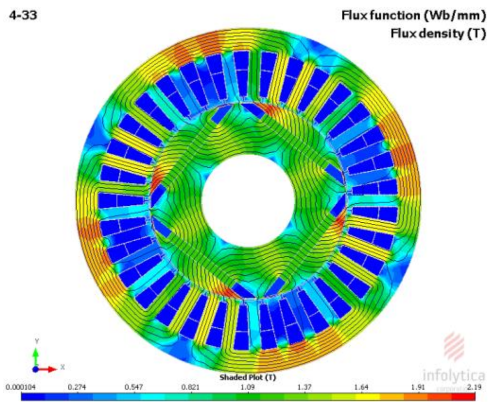

Fig. 7. Motor flux density.

To calculate the torque-speed curve, the rotor speed is varied from 10% to 150% of the rated speed, and the torque is measured at each stage. The torque-speed curve is shown in Fig. 8. According to this figure, the torque remains constant at 160 RPM and then drops.

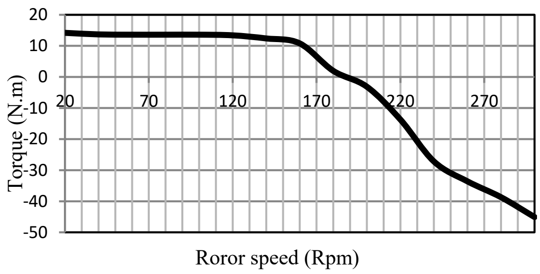

Fig. 8. Torque vs Rotor Speed.

As previously mentioned, cogging torque is an undesirable torque that should be less than 5% of the rated torque. To calculate this torque, the stator winding excitation is set to zero, and the rotor speed is considered low. The torque calculated in this state is the cogging torque [22-23]. The cogging torque curve of the motor is shown in Fig. 9. According to this figure, the maximum cogging torque is 0.003 Nm, which is 0.4% of the rated torque, making it highly desirable.

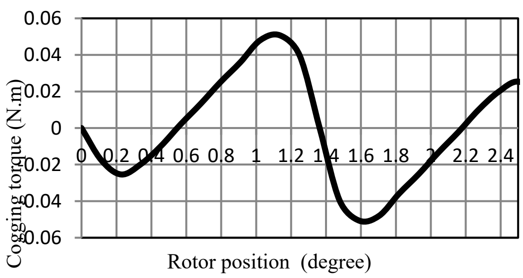

Fig. 9. Cogging torque vs Rotor position

V. Simulation

Simulation Using the results and analyses, the optimal combination of factor levels and torque values at the optimum point is calculated. According to the obtained optimum point, the necessary corrections to reach this point and the results after simulation are compared with the values obtained by the Taguchi method. - Research shows that this method is suitable for multi-objective optimization design of high-speed brushless DC motors, and in the next step, the effect of each level should be calculated separately. Also, by following this pattern, we will arrive at the values of Tables (3) and (4). In addition, according to Figure 10, the best combination for the optimum case is. The B-EMF of phases A, B and C is shown. According to this figure, the phase voltages have a 120-degree phase difference with equal amplitude. The maximum voltage is equal to the rated voltage, which confirms the correctness of the design. In addition, the line voltages of AB, BC and CA are shown on Fig.11.

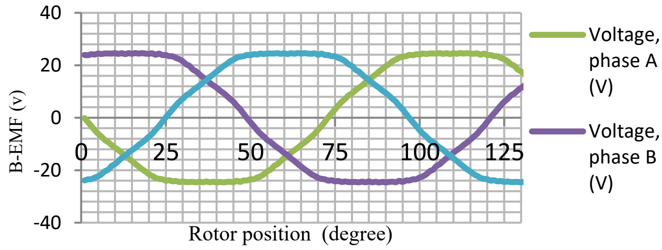

Fig. 10. B-EMF of phases A, B, and C.

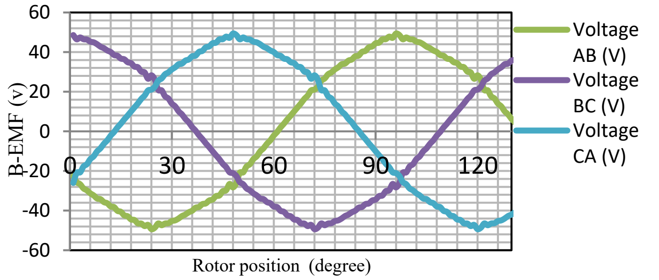

Fig.11. Line voltages of the motor.

The waveforms of the motor's torque and output power are shown in Fig. 12 and 30, respectively. According to these figures, the motor's average torque is around 12 Nm, close to the rated torque. The torque ripple in this case is 2.8 Nm, which is acceptable compared to the rated torque.

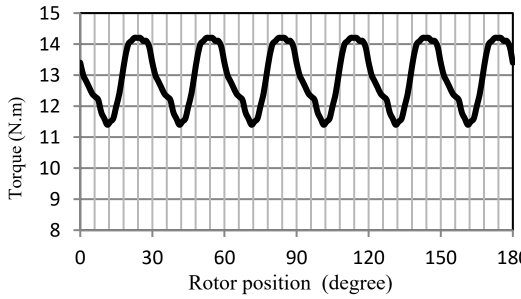

Fig. 12. Output Torque vs Rotor position

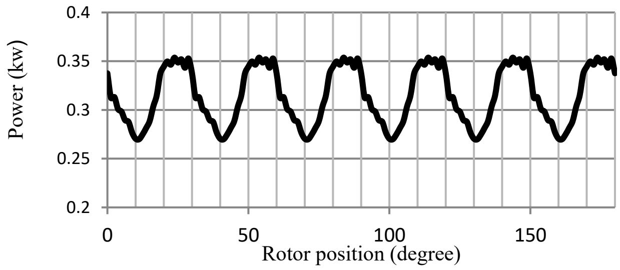

Fig. 13. Output power vs Rotor position

The losses calculated using the FEM include core losses, ohmic losses, and eddy current losses in the magnet, which are discussed in this section. When electric current passes through a conductor, it generates heat losses, known as copper losses. The copper losses are given by Eq. (1-4), where R is the DC resistance of the winding (Ω), and I is the RMS current (A) passing through the winding. Based on the phase resistance and rated current, the ohmic losses of the motor are 40W. The energy lost as heat in the motor core is referred to as core losses. The core losses calculated using the software are 4.5W.

VI. Conclusion

In this paper, the analytical method for designing a BLDC motor was thoroughly examined. Then, considering the available nominal values, the design of various four-pole motors was discussed. The outputs of these motors were compared, and it was demonstrated that the motor with four poles and 33 slots provides the best performance. Finally, the complete dimensions of this motor were presented. In third, the simulation of the designed motor was examined, and the results of the simulation were compared with the analytical results. All results were computed using Magnet software, one of the most powerful FEM software tools. A careful examination of the results reveals that the FEM-calculated values closely match the design specifications.

References

[1] Z. Chen, J. Qi, X. Chen, J. Xu, Y. Liu and Z. Dong, "Parallel Converter Cell-Based Step-Down Bridgeless PFC Converters with Wide Output for BLDC Motor," in *IEEE Transactions on Industry Applications*, vol. 61, no. 2, pp. 3293-3302, March-April 2025,

[2] T. Kim, H. Park and Y. Suh, "Fault-Tolerant Control Method Using Tangential Weighting to Improve Torque per Ampere for Medium-Voltage Drives Under Multi-Phase Open Fault Condition," in *IEEE Transactions on Industry Applications*, vol. 61, no. 2, pp. 3078-3088, March-April 2025.

[3] B. Kwon Choi *et al*., "Compensation of Scanning Speed Instability in a Wavelength-Swept Laser for Dynamic Fiber Optic Sensors," in *IEEE Sensors Journal*, vol. 25, no. 2, pp. 2784-2790, 15 Jan.15, 2025.

[4] M. Sepehrinour, H. Karimi and A. Siadatan, "Optimization and Analysis of a 50 KW Photovoltaic Power Plant with Examination of Partial Shading Conditions," *2023 25th European Conference on Power Electronics and Applications (EPE'23 ECCE Europe)*, Aalborg, Denmark, 2023, pp. 1-9.

[5] E. Chaharmahali, M. Sepehrinour, H. Karimi and A. Siadatan, "Harmonic Distortion Optimization of Multilevel H-bridge Inverter with Delta-Connected," *2023 13th Smart Grid Conference (SGC)*, Tehran, Iran, Islamic Republic of, 2023, pp. 1-5.

[6] Karimi, H.; Tarassodi, P.; Siadatan, A.; Sepehrinour, M. Designing and Manufacturing a Solar Tracking of Photovoltaic (PV) Panels for Produce Maximum Power Electrical. In Proceedings of the International Symposium on Power Electronics, Electrical Drives, Automation and Motion, SPEEDAM, 2024; pp. 498–502.

[7] M. M. Hayati, A. Aminlou, K. Zare, H. Karimi, A. Siadatan and M. Abapour, "Power Distribution Network Reconfiguration Based on Energy Loss Reduction using Graph Theory," Journal of Energy Management and Technology, (2025), doi: 10.22109/jemt.2025.478238.1526.

[8] A. Siadatan, H. Karimi, P. Tarassodi and M. Sepehrinour, "Recycling the Driving Force of a Hybrid Electric Bicycle in the Drive Cycle in Order to Provide Energy in Negative Slopes," *2024 International Symposium on Power Electronics, Electrical Drives, Automation and Motion (SPEEDAM)*, Napoli, Italy, 2024, pp. 1036-1041.

[9] H. Karimi, P. Tarassodi, A. Siadatan and M. Sepehrinour, "Control of Reactive Power and Connection Voltage in Grid Connected Wind Turbine," *2024 International Symposium on Power Electronics, Electrical Drives, Automation and Motion (SPEEDAM)*, Napoli, Italy, 2024, pp. 503-508,

[10] M. Asgar, A. Siadatan and E. Afjei, "A swappable single phase switched reluctance motor with bifilar drive converter," *2012 3rd Power Electronics and Drive Systems Technology (PEDSTC)*, Tehran, Iran, 2012, pp. 261-265.

[11] F. Ghalavand and T. Ilamparithi, "High-Performance Spoke-Type PMSM Rotor for High-Torque, Low-Speed Applications," 2025 IEEE/AIAA Transportation Electrification Conference and Electric Aircraft Technologies Symposium (ITEC+EATS), Anaheim, CA, USA, 2025, pp. 1-6.

[12] R. Sharifi Shahrivar , H. Gholizadeh , A. Siadatan and S. E. Afjei, "Design and Implementation of a Modified Boost Topology with High Voltage Ratio and Efficiency Besides the Lower Semiconductors Stresses," International Journal of Research and Technology in Electrical Industry, 2 1 (2023): 67-76,

[13] A. A. Khan etal, "Single-Stage Bidirectional Buck–Boost Inverters Using a Single Inductor and Eliminating the Common-Mode Leakage Current," *IEEE Trans. Power Electron*, vol. 35, no. 2, pp. 1269-1281, Feb. 2020.

[14] A. R. Kazemi, M. Asgar, E. Afjei and A. Siadatan, "A new rotor position detection method using bifilar windings and resonant circuit in SRM drive," *2010 IEEE International Conference on Power and Energy*, Kuala Lumpur, Malaysia, 2010, pp. 744-748,

[15] H. Torkaman, M. Fakhari, H. Karimi and B. Taheri, "New Frequency Modulation Strategy with SHE for H-bridge Multilevel Inverters," *2018 4th International Conference on Electrical Energy Systems (ICEES)*, Chennai, India, 2018, pp. 157-161.

[16] S. Esmaeili, S. Karimi, P. Tarassodi and A. Siadatan, "Two-stage asymmetrical Γ-Z-source inverter with high voltage gain and reduced shoot-through duty ratio," *2016 International Symposium on Power Electronics, Electrical Drives, Automation and Motion (SPEEDAM)*, Capri, Italy, 2016, pp. 956-961.

[17] E. Afjei, A. Siadatan, A. Rezaei-Zare and H. Gholizadeh, "A Quadratic Boost Converter with Continuous Input Current and Low Normalized Voltage/Current Stresses," *2022 International Symposium on Power Electronics, Electrical Drives, Automation and Motion (SPEEDAM)*, Sorrento, Italy, 2022, pp. 395-401.

[18] S. Esmaeili, S. Karimi, A. Mostaan, A. Iqbal and A. Siadatan, "A Family of High Step-Up A-Source Inverters with Clamped DC-Link Voltage," *2019 10th International Power Electronics, Drive Systems and Technologies Conference (PEDSTC)*, Shiraz, Iran, 2019, pp. 195-200.

[19] Alireza Siadatan, Hamed Karimi, Maryam Sepehrinour. Construction and Application of a Five-Level Inverter for Maximum Power Point Tracking (MPPT) of the Photovoltaic Systems (PV). *The 26th European Conference on Power Electronics and Applications*, GDR SEEDS France & EPE Association, Mar 2025, Paris, France.

[20] A. Moraveji, A. Siadatan, E. Afjei, M. Rafiee and E. Z. A. Abadi, "DSP sensorless controller of Switched Reluctance Motor-Generator approaching to AM modulation," *2012 4th International Conference on Intelligent and Advanced Systems (ICIAS2012)*, Kuala Lumpur, Malaysia, 2012, pp. 424-428.

[21] H. Karimi, A. Siadatan and A. Rezaei-Zare, "A Hybrid P&O-Fuzzy-Based Maximum Power Point Tracking (MPPT) Algorithm for Photovoltaic Systems under Partial Shading Conditions," in *IEEE Access*, doi: 10.1109/ACCESS.2025.3533314.

[22] A. Siadatan, H. Karimi, P. Tarassodi and M. Sepehrinour, "Optimization and Performance of Transformer Temperature Under Harmonic Conditions with Various Windings," *2024 International Symposium on Power Electronics, Electrical Drives, Automation and Motion (SPEEDAM)*, Napoli, Italy, 2024, pp. 123-128.

[23] A. R. Kazemi, M. Asgar, E. Afjei and A. Siadatan, "A novel sensorless method for rotor position detection in bifilar SRM drive," *2010 IEEE International Conference on Power and Energy*, Kuala Lumpur, Malaysia, 2010, pp. 438-443.

979-8-3315-8138-1